Ferroelectric Behavior of an Octahedral Metal-Ligand Cage and Its 2D-Connected Cage Framework

Neetu Prajesh, Ashok Yadav, Rani Gourkhede, Balu Praveenkumar, Alexander Steiner, Ramamoorthy Boomishankar

Abstract

Supramolecular systems hold great potential as ferroelectric materials because they are easy to prepare and do not require toxic and environmentally damaging elements. However, directing the self-assembly process of a supramolecular array to yield polarizable solids is still challenging. Here, we describe induced ferroelectricity in a supramolecular framework of metal-organic cages that are supported by a flexible tripodal ligand $(NHCH_2\text{-}(3\text{-}Py))_3PO$ (TPPA). Ferroelectric responses on the discrete cage $[Cu_6(H_2O)_{12}(TPPA)_8](NO_3)_{12} \cdot 45H_2O$ (**1**) and its 2D-connected framework $[\{Cu_6Cl_4(H_2O)_6(TPPA)_8\}(NO_3)_8 \cdot 60H_2O]_n$ (**2**) yielded well-resolved rectangular hysteresis loops at room temperature with remnant polarization values of 27.27 and 29.09 μC/cm^2, respectively. Thermal hysteresis measurements (THM) and capacitance-voltage (C−V) plots further corroborate the ferroelectric behavior in these compounds. The polarization in them is due to the displacements of solvated molecules and nitrate ions in the pockets of these frameworks.

Introduction

Ferroelectricity is the property of polar crystalline substances exhibiting spontaneous electric polarization, which can be reversed by sweeping the direction of the electric field.[1] Ferroelectric materials find many technological applications, such as in memory devices and sensors.[2-5] Recent studies explored ferroelectrics as solar- and mechanical-energy harvesting systems.[6-9] Most commercial ferroelectrics utilize ceramic metal oxide systems.[10-12] However, these materials are mostly brittle, require high processing temperatures and often contain heavy and toxic elements. Aiming to overcome these issues, molecular and polymeric systems have been explored to achieve better flexibility, light weight character, low temperature synthesis and processing techniques.[13-21] Metal-organic frameworks are promising ferroelectrics because of the many ways in which their structures can be constructed and modified.[22, 23] However, uncovering the mechanism behind their ferroelectric behavior is challenging because of the complexity of their structures.[6, 24-26]

Our group has been interested in the ferroelectric behavior of metal-organic assemblies supported by di- and tripodal phosphoramide ligands of the type $[PhPO(NHPy)_2]$, (Py=3-pyridyl (^{3}Py) or 4-pyridyl (^{4}Py)) and $[PS(NH^3Py)_3]$.[6, 27, 28] We were able to obtain axially symmetric octahedral M_6L_8 cages using the tripodal $[PS(NH^3Py)_3]$ ligand and reversibly connect these cages to form hierarchical frameworks of discrete, 1D, 2D and 3D-structures.[26] While the discrete and 1D-frameworks exhibited ferroelectric behavior, this could not be established for the 2D and 3D-frameworks of this series since these were plagued by poor crystal quality that hampers the electrical measurements on them. Hence, we focused on the design of new ligands to improve the structural integrity and the ferroelectric response of these materials. Herein, we report the synthesis and ferroelectric behavior of the octahedral cage assembly $[Cu_6(H_2O)_{12}(TPPA)_8](NO_3)_{12} \cdot 45H_2O$ (**1**) and its 2D-cage connected

framework $[\{Cu_6Cl_4(H_2O)_6(TPPA)_8\}(NO_3)_8 \cdot 60H_2O]_n$ (**2**). These are supported by the tris(N-(3-picolyl))phosphoramide ligand $(NHCH_2\text{-}(3\text{-}Py))_3PO$ (TPPA). The ligand is more flexible due to the introduction of internal CH_2 groups that connect the bridge-head P=O unit with the three coordinating pyridyl rings. Crystals of **1** and **2** gave the remnant polarization (P_r) values of 27.27 and 29.09 $\mu C/cm^2$, respectively. This is the first report on the observation of ferroelectric behavior in a 2D-framework of octahedral cages. The observation of ferroelectric behavior in these cage-derived systems reinforces the effect of disordered anions and solvates in governing the polarization in supramolecular metal-ligand systems.

Results and Discussion

The ligand TPPA was synthesized by refluxing 3-picolylamine and $POCl_3$ in toluene (Scheme 1). The ^{31}P NMR of the ligand yields a single signal at δ 16.78 ppm while MALDI-TOF spectra showed m/z values of 391.12 and 407.19 corresponding to [M+Na] and [M+K] ions (See Figures S1-S3, Supporting Information for full characterization including single crystal structure analysis). Treatment of TPPA with $Cu(NO_3)_2 \cdot 3H_2O$ in 1 : 3 ratio in MeOH/H_2O mixtures gave $[Cu_6(H_2O)_{12}(TPPA)_8](NO_3)_{12} \cdot 45H_2O$ (**1**), which consists of discrete octahedral cages. Reaction of **1** with NaCl in MeOH/H_2O yielded the 2D-connected cage framework $[\{Cu_6Cl_4(H_2O)_6(TPPA)_8\}(NO_3)_8 \cdot 60H_2O]_n$ (**2**); in it every cage is connected to four others via chloride bridges between Cu(II) centers. Both **1** and **2** were obtained as blue crystals from the slow evaporation of their reaction mixtures (Scheme 1).

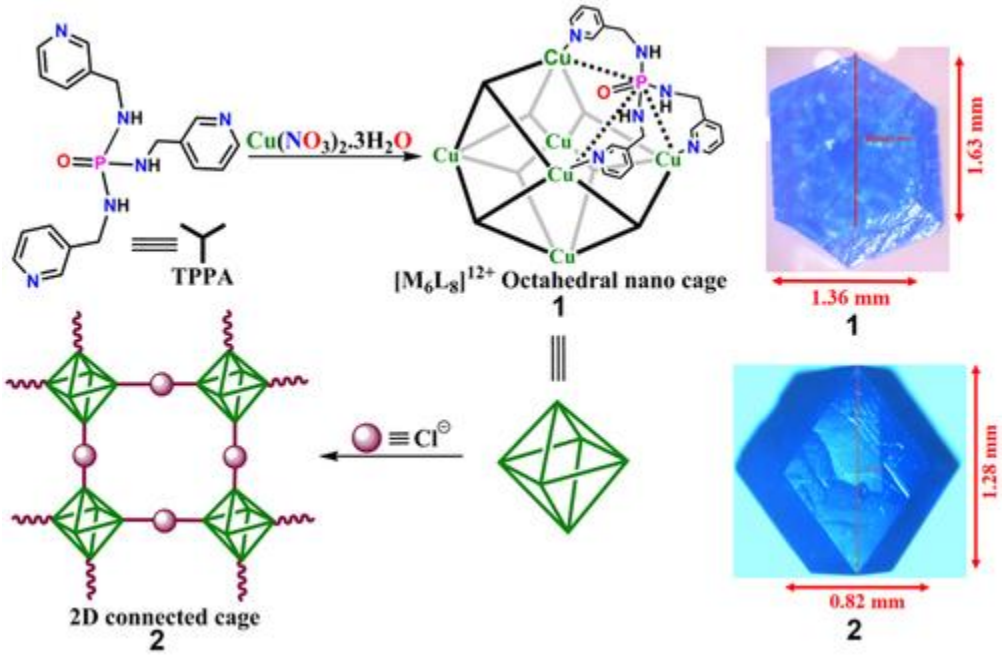

Scheme 1. Schematic diagram showing the formation of cage **1** and its 2D-connected cage framework **2**. Images of the crystals of **1** and **2** under the microscope and their dimensions are given on the right side.

Single crystal X-ray structure analysis reveals that compound **1** crystallizes in cubic space group *P*n-3n. Each Cu(II) center of the cationic cage $[Cu_6(H_2O)_{12}(TPPA)_8]^{12+}$ shows a Jahn-Teller-distorted octahedral coordination (Figure 1a and Supporting Information, Figures S4-S5). Its equatorial positions are occupied by the N-atoms of four TPPA ligands while the axial positions bind two water molecules. The discrete cages have chiral octahedral symmetry (point group O). The six Cu^{2+} ions coincide with the 4-fold rotation axes while the TPPA

ligands occupy the 3-fold rotation axes. The P=O groups are oriented towards the cavity of the cage. Hence, the crystal is a racemate containing cages of opposite handedness, which form a cubic pseudo-body-centered packing (Figure 1b and Supporting Information, Figure S6). The solvent accessible volume of the cavity inside the cage measures 436 $Å^3$ which is 7.0% of the total volume (Supporting Information, Figure S7a). It is occupied by disordered water molecules forming a cage like hydrogen bonded network that is connected to the P=O groups and the copper bound water molecules (Supporting Information, Figure S8). However, the bulk of the void volume is found between the cages. It forms an extended 3D-channel structure that occupies 39.4% of the total volume; it contains nitrate anions and water molecules (Supporting Information, Figure S7b). They form a hydrogen bonded network that also involves cage bound NH groups and Cu-coordinated water ligands (Figure 1c and Supporting Information, Figure S9). The contents of both internal and external voids are highly disordered.

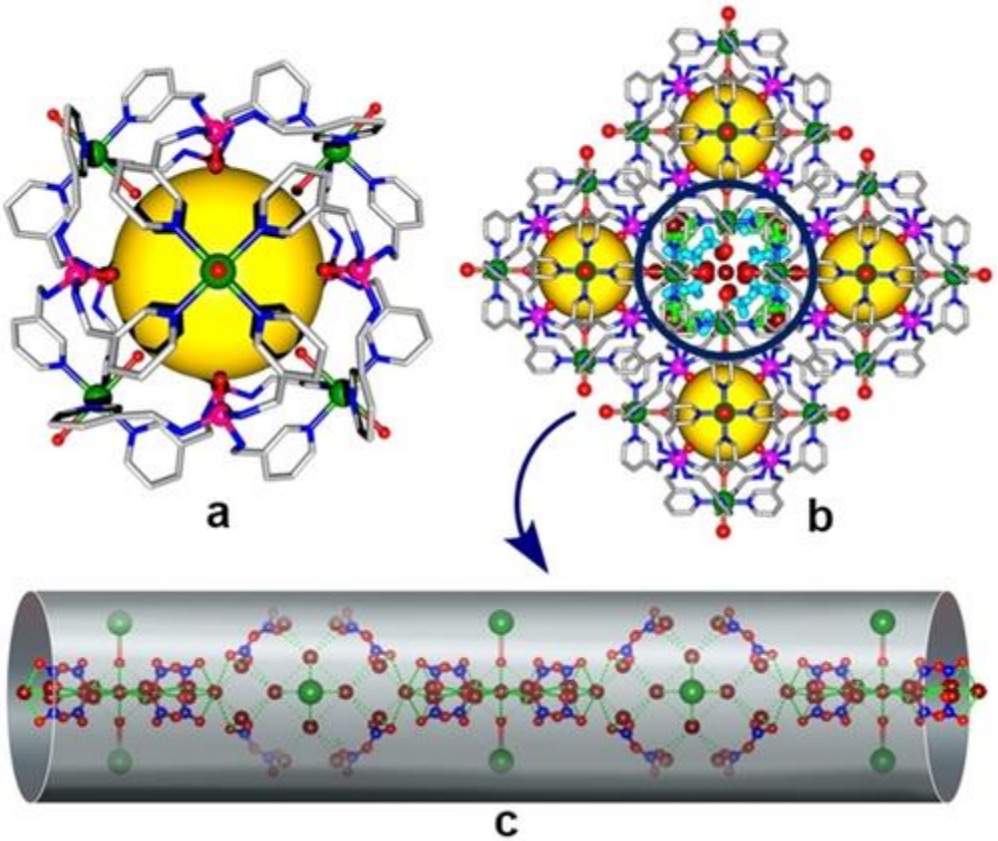

Figure 1. (a) Octahedral core structure of **1**. (b) Packing view of **1** showing the extrinsic voids filled with disordered nitrate anions and solvated water molecules. (c) Closer view of the H-bonded chains of nitrate anions and water molecules (both solvated and coordinated) that are responsible for the long-range polar order.

Crystals of **2** exhibit space group symmetry *I*422. The cages are linked via Cu−Cl-Cu bridges resulting in a two-dimensional square-grid type framework (Figure 2a). These grids are packed on top of each other so that nodes of one layer sit above squares of the next layer resembling the layered structure of SnF_4 (I4/mmm), (Supporting Information, Figure S10).[29] The homochiral nature of the grid shows that the handedness is passed on from one cage to another via the chloride bridges. Neighboring layers have the same handedness which contrasts the racemic nature of the earlier reported 2D-framework that is supported by ligands $PS(NH^3Py)_3$ (Supporting Information, Figure S11).[27] Crystals of **2** have the composition

$[\{Cu_6Cl_4(H_2O)_6(TPPA)_8\}(NO_3)_8 \cdot 60H_2O]_n$. The two non-bridging Cu-coordination sites are occupied by water molecules. The endo sites bind chloride and water molecules with varying site-occupancies. As a result, the inside void of the cages is slightly smaller than **1** and measures 371 $Å^3$ (6.1% of total volume), while the external void volume, which again forms a 3D-channel network, makes up 37.1% of the total volume (Supporting Information, Figure S12). Similar as in **1** the inner voids are filled with water molecules, while the external channels contain nitrate ions and water molecules. Again, the contents of the voids are highly disordered; nitrate ions are distributed over two sites in pockets of the hydrogen bonded network (Figure 2b and Supporting Information, Figure S13).

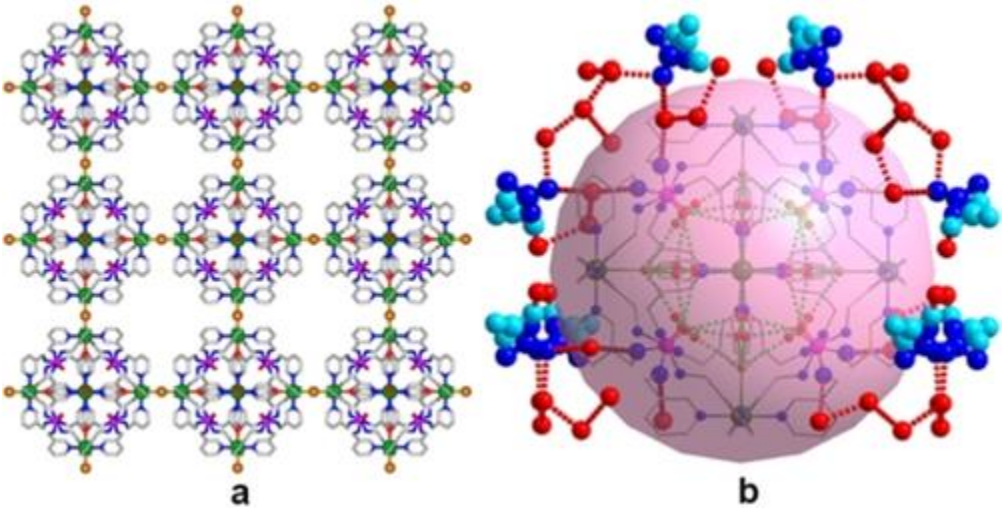

Figure 2. (a) View of the 2D-framework in **2** along the c-axis. b) View of disordered nitrate ions at the extrinsic pores of **2** and their interactions with disordered water molecules.

The polarization in these compounds result from the toggling of nitrate ions as part of a hydrogen-bonded network with water molecules hosted by the mainly static framework of cages. It should be pointed out that the non-polar space groups of these compounds only reflect the symmetry of the rigid frameworks of cages, but not the disordered ions and molecules occupying the void spaces. Attempts to resolve the disorder by performing X-ray diffraction on polarized crystals remained futile due to the very low scattering contributions and diffuse character of nitrate ions and water molecules occupying the voids. The P−E hysteresis loops of **1** and **2** were measured on single crystals by using a Sawyer-Tower circuit at room temperature. For **1**, the measurements can be performed along any of the two opposite crystal faces due to its cubic symmetry. The measurements on **2** were performed across the larger face that coincides with the [1 0 −1] plane (Supporting Information, Figure S14). The nitrate anions and H-bonded solvated water molecules run parallel to this plane giving rise to long-range polar order that is reversible (Figure 2b).

The P−E loop measured on single crystals of **1** at 0.1 Hz shows a high remnant polarization (P_r) value of 27.27 $\mu C/cm^2$ (Figure 3a). The plot of current density (J) vs. electric field (E) gives two opposite peaks at the coercive fields (E_c) corresponding to two stable states with opposite polarity. Based on the J−E curves, the saturation polarization (P_s) and the coercive field (E_c) were found to be 25.91 $\mu C/cm^2$ and 0.22 kV/cm, respectively. Similar measurements on **2** at 0.1 Hz, gave a P_r value of 29.09 $\mu C/cm^2$ at room temperature. Also, from the obtained J−E curves, the P_s and E_c values were estimated to be 26.79 $\mu C/cm^2$ and 0.56 kV/cm, respectively (Figure 3b). The considerably small coercive fields (E_c) suggest swift switching of the ferroelectric domains in both these crystals. As observed in most

supramolecular ferroelectrics, the obtained P_r values are smaller than the P_s for both **1** and **2**. Normally, the elastic energy of the bonds plays a vital role in domain evolution and the field dependent polarization switch. As a result, the supramolecular ferroelectrics based on weak interactions may often exhibit higher P_r than P_s due to the slower switching of polarization in comparison with those of the conventional oxide ferroelectrics.[30]

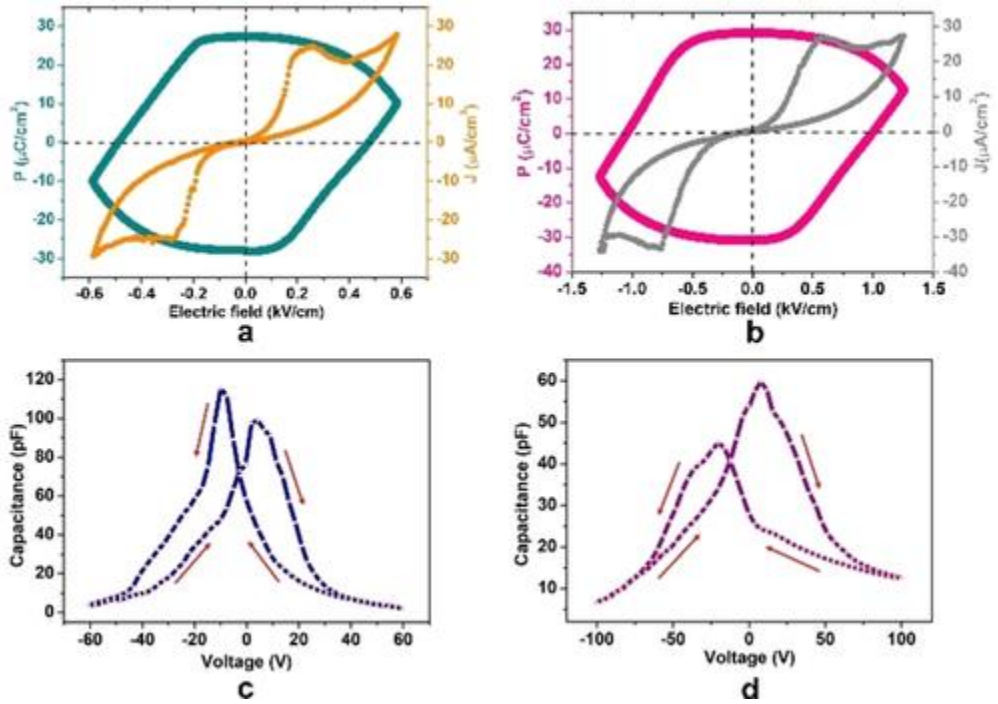

Figure 3. P−E hysteresis loop and the corresponding leakage current plots for the single crystals of (a) **1** and (b) **2**. The C−V curves of (c) **1** (d) **2**.

In addition to the P−E hysteresis curves, capacitance vs. voltage (C−V) curves were also measured for both these assemblies. The C−V characteristics were measured by sweeping the voltages up and down between 0 and ±60 V and 0 and ±100 V, respectively, on the crystals of **1** and **2** (Figures 3c and 3d). During the measurements, the capacitance peaks are observed upon ramping up the dc voltages and are absent when the dc voltages are brought down. Also, the C−V curves of **1** and **2** indicate hysteresis behavior with a characteristic butterfly like shape because of the reversal of polarization direction in the developed domain structure. The voltages corresponding to the capacitance peaks are related to the coercive field while the polarization switching matches closely with those obtained in their corresponding P−E loops and J−E curves. The switching asymmetry observed in the P−E loops and J−E curves can also be seen in the obtained C−V curves.[31-33]

The ferroelectric fatigue measurements on the crystals of **1** and **2** shows the retention of more than 50% of the P_r values even after 10^4 switching cycles (Figures 4a). Furthermore, the temperature dependent P−E hysteresis loop measurements supported the ferroelectric nature of the obtained P−E loops in **1**. For this, the thermal hysteresis measurement (THM) data were obtained on **1** in which remnant polarization is measured against temperature. Generally with increase in temperature, the P_r decreases. However, the polarization in **1** increases from 7.25 to 28.83 μC/cm^2 at 0.8 Hz along the same driving voltage when the temperature is increased from 299.5 K to 321.7 K (Figures 4b). Such increments in P_r may be attributed to the alignment of some randomly oriented domains with rising temperature.[34] With further increase in temperature, crystals develop cracks and loss of crystallinity. For **2**, such

measurements gave inconsistent values probably due to the random loss of solvates upon heating the sample. In addition, room temperature second harmonic generation (SHG) experiments were performed on the finely grounded and unsieved powder samples of cages. The observed SHG efficiencies of 7.2% and 9.0% for **1** and **2**, respectively, corresponding to the standard potassium dihydrogen phosphate (KDP) sample confirms the ferroelectric nature of these materials.

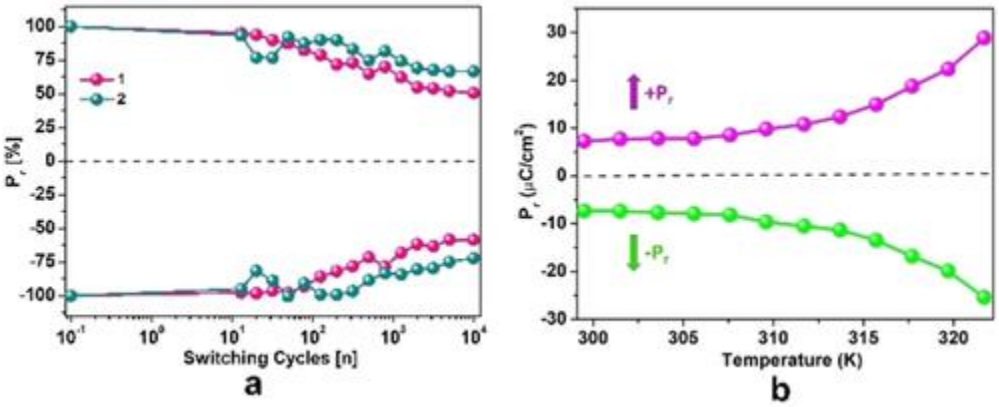

Figure 4. (a) Ferroelectric fatigue data for **1** and **2**. (b) Observed trends in the obtained remnant polarization (P_r) values of **1** as a function of temperature from the thermal hysteresis measurement (THM).

The temperature dependent dielectric permittivity measurements were carried out at various frequencies in the range of 10^3 – 10^6 Hz on compact polycrystalline pellets of **1** and **2**. Figures 5a and 5b shows the dielectric curves for **1** and **2** with the anomaly peaks centered on 353 and 363 K, respectively. As with other similar cages,[26] the broad nature of these anomaly peaks is attributed to the desolvation of the framework. The observed ϵ' values at 1 kHz for **1** and **2** at 298 K are 55 and 32, respectively, shooting up to 635 and 111 at their respective anomaly points. The motional dynamics of the polar water molecules and the anions located in the pockets of cages could, in principal, result in such high dielectric constant values at higher temperatures.[35, 36] Furthermore, the frequency independent behavior of the anomaly peaks implies that both **1** and **2** behave as relaxor-free dielectric materials. The plot of ϵ' vs. frequency for **1** and **2** shows a decreasing trend in the dielectric permittivity values with increasing frequencies indicating the engagement of all polarization mechanisms (Supporting Information, Figures S15-S16,).[1, 37] The corresponding dielectric loss (tan δ) plots also follow the same trend and support the high dielectric and ferroelectric nature of these assemblies (Supporting Information, Figures S17–S20).

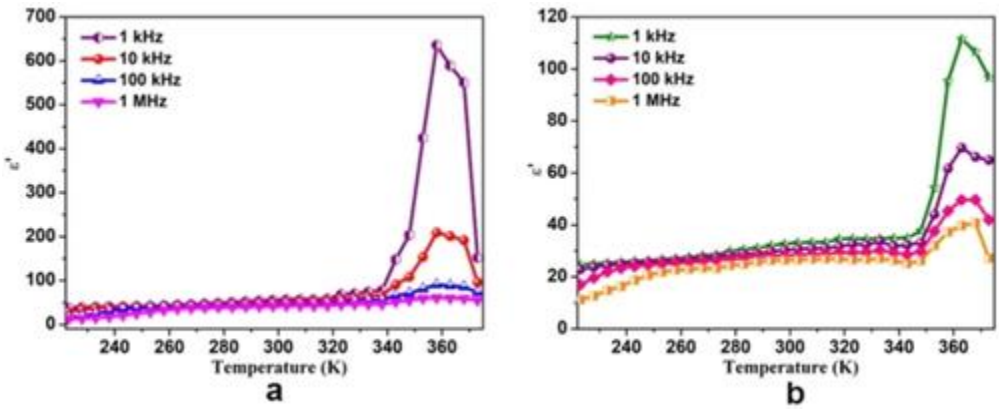

Figure 5. Plots of real part of dielectric permittivity as a function of temperature for (a) **1** and (b) **2**.

In contrast to the previously reported cages,[26, 28] the desolvation assisted dielectric transitions in **1** and **2** occur over much narrower temperature ranges. Variable temperature PXRD measurements on the bulk samples of **1** and **2** indicate loss of crystallinity above the transition temperatures. The crystallinity, however, is restored after a few drops of the mother liquor were added (Figure 6 and Supporting Information, Figure S21). The reversible switching between solvated crystalline and desolvated amorphous phases is mirrored in the FT-IR spectra recorded in the ATR mode. They show signals in the region of 3600–3100 cm^{-1} due to solvated molecules of water, which mostly disappear in the desolvated phase, but then re-emerge to their original intensity upon addition of mother liquor (Supporting Information, Figures S22–S23). The 298 K single-crystal X-ray diffraction analyses of **1** and **2** indicate that the space group symmetries of their crystals remain unchanged and their unit cell parameters were closely similar to those obtained from 100 K data. In fact, the crystal structure of **1** could be solved at 298 K that shows large thermal ellipsoids particularly to the organic parts of the molecule (Supporting Information, Table S2-S3 and Figure S24).

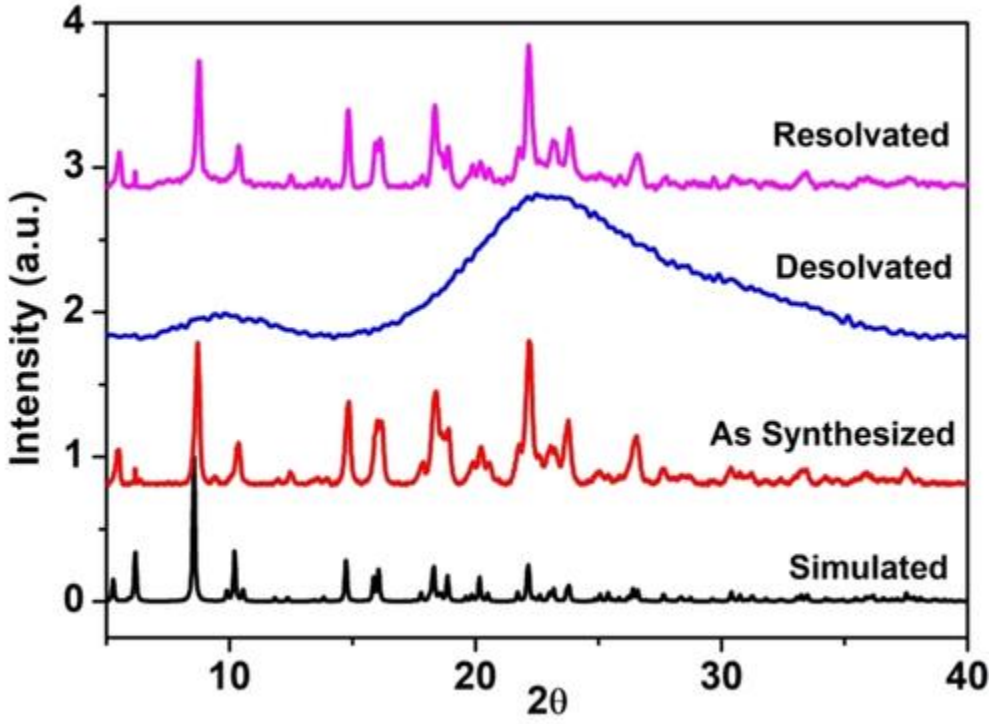

Figure 6. Powder X-ray diffraction (PXRD) pattern for the various samples of **2**.

The TGA of **1** and **2** shows the initial weight loss of around 18% at 70 °C due to the loss of both solvated and coordinated water molecules. Both **1** and **2** were found to be stable up to 170 °C. The TGA of the desolvated samples of **1** and **2** ($\mathbf{1}_{desolvated}$ and $\mathbf{2}_{desolvated}$) shows no major weight losses at the initial temperatures and shows the stability of the frameworks up to 170 °C. However, the original TGA profiles of **1** and **2** were almost restored upon resolvation by adding a few drops of their corresponding mother liquor. (Supporting Information, Figures S25–S28). Furthermore, the P−E loop measurements performed on compacted pellet samples of $\mathbf{1}_{desolvated}$ and $\mathbf{2}_{desolvated}$ shows resistor-type behaviour, signifying the role of the solvate molecules in the packing structure of **1** and **2** in restoring the long-range order responsible for their ferroelectric polarization (Supporting Information, Figures S29).[28]

Conclusion

In conclusion, we have synthesized an octahedral Cu_6L_8 cage containing the more flexible tripodal tris(N-(3-picolyl))phosphoramide ligand. Formation of the 2D-framework was achieved by introducing bridging chloride ions. Both **1** and **2** showed ferroelectric response due to the toggling of nitrate anions within a hydrogen bonded network with water molecules. The observed P_r values of 27.27 μC/cm^2 (**1**) and 29.09 μC/cm^2 (**2**) are consistent with those reported for similar types of cage compounds. The ferroelectric nature in **1** and **2** were further confirmed by butterfly-like hysteresis loops obtained in C−V measurements as well as by the thermal hysteresis measurements in the case of **1**. The observation of high dielectric constants supports the presence of stable dipoles in both of these assemblies. These results shed further light on the role of unconventional type of mechanisms such as toggling of anions that control the origin of ferroelectric behavior in metal-ligand assemblies.

Experimental Section

Materials and characterization: All manipulations involving phosphorous halides were performed under dry nitrogen or argon atmosphere in standard Schlenk-glassware. The solvent toluene was dried over sodium. 3-picolylamine was purchased from Aldrich and used as received. $POCl_3$ was purchased locally and was distilled prior to use. $Cu(NO_3)_2 \cdot 3H_2O$ was purchased from Aldrich and used as received. NMR spectra were recorded on a Jeol 400 MHz spectrometer (^{1}H NMR, 400.13 MHz; ^{13}C{^{1}H} NMR, 100.62 MHz; ^{31}P{^{1}H} NMR, 161.97 MHz) at room temperature using $SiMe_4$ (^{1}H, ^{13}C) and 85% H_3PO_4 (^{31}P). The MALDI-TOF spectra were obtained on an Applied Biosystem MALDI-TOF/TOF spectrometer. The powder X-ray diffraction (PXRD) data were obtained from a Bruker-D8 Advance diffractometer. Thermal analysis (TGA) data have been obtained from a Perkin-Elmer STA-6000 thermogravimetric analyzer. The measurement of the second harmonic generation was carried out by using the method of Kurtz and Perry. The fundamental wavelength is 1064 nm generated by a Q-switched Nd:YAG laser with a frequency doubling at 532 nm. The samples were filled into a capillary tube and a powdered potassium dihydrogen phosphate (KDP) sample was used as the reference. Elemental analyses were performed on a Vario-EL cube elemental analyzer. FT-IR in attenuated total reflectance (ATR) mode was taken on neat samples on a Bruker Alpha spectrophotometer. Melting points were obtained using an Electro thermal melting point apparatus and were uncorrected.

Synthesis of tris(N-(3-picolyl))phosphoramide (TPPA): To a stirred solution of 3-picolylamine (3.80 mL, 4.042 g, 37.38 mmol) in toluene (~100 mL) at 0 °C, $POCl_3$ (0.5 mL, 0.82 g, 5.34 mmol) in 10 mL of toluene was added drop wise through a pressure equalizer funnel and the reaction mixture was refluxed for overnight until a white precipitate was formed. The toluene was decanted and the solids were extracted in dichloromethane three times. The combined dichloromethane extracts were evaporated under reduced pressure to yield the pure ligand. Crystals of TPPA were obtained by slow evaporation of a solution from methanol. Yield: 1.56 g (79.18%). M.P.: 105–110 °C. ^{1}H NMR ($CDCl_3$): δ 8.45 (d, 3H, CH(pyridyl)), δ 8.34 (dd, 3H, CH(pyridyl)), δ 7.56 (td, 3H, CH (pyridyl)), δ 7.12 (dd, 3H, CH (pyridyl)), δ 4.07 (t, 3H, NH), δ 3.59 (d, 6H, CH_2). ^{13}C {^{1}H} NMR ($CDCl_3$): δ 42.77, 123.63, 135.36, 135.88, 148.53, 148.87. ^{31}P NMR (162 MHz,{$(CD_3)_2SO$}): δ 16.78. MALDI-TOF: 391.12 $(M+Na)^+$, 407.09 $(M+K)^+$ Anal. Calcd. for $C_{18}H_{21}N_6OP$: C, 58.69; H, 5.75; N, 22.81. Found: C, 56.38; H, 3.26; N, 20.89.

Synthesis of Compound 1: To a stirred solution of TPPA (50 mg, 0.135 mmol) in MeOH (3 mL), $Cu(NO_3)_2 \cdot 3H_2O$ (98.25 mg, 0.407 mmol) in H_2O was added. An initially formed bluish green precipitate was dissolved by adding water (2-3 drops) giving rise to a blue-colored solution. The resulting solution was stirred for 2 h and was filtered through a thick pad of celite. Blue crystals suitable for SCXRD analysis were obtained from the filtrate after five days. Yield: 80%. M.P. 82–87 °C. FT-IR data on powder (cm^{-1}): 3457, 3238, 1601, 1425, 1314, 1178, 1079, 882, 784, 702, 599, 552. Anal. Calcd. for $C_{144}H_{282}N_{60}O_{101}P_8Cu_6$: C, 33.92; H, 5.57; N, 16.48. Found: C, 32.26; H, 2.32; N, 15.10.

Synthesis of Compound 2: To a stirred solution of TPPA (50 mg, 0.135 mmol) in MeOH (3 mL), $Cu(NO_3)_2.3H_2O$ (98.25 mg, 0.407 mmol) in H_2O (0.5 mL) was added. An initially formed bluish green precipitate was dissolved by adding water (2-3 drops) giving rise to a blue-colored solution. After 30 minutes of stirring, an aqueous solution of NaCl (excess) was added to the mixture. The resulting solution was stirred for 2 h and was filtered through a thick pad of celite. Blue crystals suitable for SCXRD analysis were obtained from the filtrate after five days. Yield: 85%. M.P. 92–98 °C. FT-IR data on powder (cm^{-1}): 3431, 3230, 1606, 1423, 1329, 1166, 1096, 874, 794, 698, 640. Anal. Calcd. for $C_{144}H_{300}Cl_4N_{56}O_{98}P_8Cu_6$: C, 33.55; H, 5.87; N, 15.22. Found: C, 32.72; H, 4.72; N, 16.08.

Crystallography: Reflections were collected on a Bruker Smart Apex Duo diffractometer at 100 K using MoKα radiation (λ=0.71073 Å). Structures were refined by full-matrix least squares against F^2 using all data using SHELX.[38] All non-hydrogen atoms were refined anisotropically if not stated otherwise. The phosphoryl oxygen atom in **2** is disordered over two sites. The nitrates ions in the asymmetric units of both **1** and **2** were disordered. The disordered fragments were refined with the similar distances and the similar U-restraints by using the SIMU/SAME command of the Shelx. Crystals of **1** and **2** were weakly diffracting at higher angles and hence their data were truncated to 2θ=50°. Hydrogen atoms were constrained in geometric positions to their parent atoms.

Ferroelectric and Dielectric measurements: The ferroelectric hysteresis loops for **1** and **2** were measured on single crystals of dimensions 1.36×1.63×0.65 and 1.28×0.82×0.60 mm, respectively, by using a Sawyer-Tower circuit. The measurements pertaining to the polarization and fatigue cycles were recorded using hysteresis loop analyzer (TF Analyzer 2000E, aixACCT, Germany). Leakage currents were measured dynamically for various voltage steps during the hysteresis loop measurements. Powder samples of **1** and **2** were compacted in the form of discs (of approximately 10 mm diameter and 1 mm thickness) to measure dielectric properties. The compacted discs were subsequently electroded using aluminum adhesive foils for both measurements. The dielectric characteristics for **1** and **2** were measured using the Novocontrol, Dielectric Spectrometer.

Acknowledgements

This work was supported by SERB, India via Grant Nos. CRG/2019/004615 (R.B.) and EMR/2016/000614 (R.B.) and Nanomission Project, DST, India via Grant No. SR/NM/TP-13/2016 (R.B.). N.P. thanks the CSIR, India for the fellowship.

Conflict of interest

The authors declare no conflict of interest.

References

1 M. E. Lines, A. M. Glass *Principles and Applications of Ferroelectrics and Related Materials*, Oxfor d university press, New York, **1977**.

2 S. Das, J. Appenzeller, *Nano Lett.* 2011, **11**, 4003–4007.

3 C. A. P. de Araujo, J. D. Cuchiaro, L. D. McMillan, M. C. Scott, J. F. Scott, *Nature* 1995, **374**, 627–629.

4 L. W. Martin, A. M. Rappe, *Nat. Rev. Mater.* 2016, **2**, 16087.

5 Y. Yuan, Z. Xiao, B. Yang, J. Huang, *J. Mater. Chem. A* 2014, **2**, 6027–6041.

6 A. Yadav, A. K. Srivastava, P. Kulkarni, P. Divya, A. Steiner, B. Praveenkumar, R. Boomishankar, *J. Mater. Chem. C* 2017, **5**, 10624–10629.

7 T. Vijayakanth, A. K. Srivastava, F. Ram, P. Kulkarni, K. Shanmuganathan, B. Praveenkumar, R. Boomishankar, *Angew. Chem. Int. Ed.* 2018, **57**, 9054–9058; *Angew. Chem.* 2018, **130**, 9192–9196.

8 T. Vijayakanth, F. Ram, B. Praveenkumar, K. Shanmuganathan, R. Boomishankar, *Chem. Mater.* 2019, **31**, 5964–5972.

9 S. Deswal, S. K. Singh, P. Rambabu, P. Kulkarni, G. Vaitheeswaran, B. Praveenkumar, S. Ogale, R. Boomishankar, *Chem. Mater.* 2019, **31**, 4545–4552.

10 B. H. Park, B. S. Kang, S. D. Bu, T. W. Noh, J. Lee, W. Jo, *Nature* 1999, **401**, 682–684.

11 R. Ramesh, J. Lee, T. Sands, V. G. Keramidas, O. Auciello, *Appl. Phys. Lett.* 1994, **64**, 2511–2513.

12 J. Zylberberg, A. A. Belik, E. Takayama-Muromachi, Z.-G. Ye, *Chem. Mater.* 2007, **19**, 6385–6390.

13 S. Horiuchi, F. Ishii, R. Kumai, Y. Okimoto, H. Tachibana, N. Nagaosa, Y. Tokura, *Nat. Mater.* 2005, **4**, 163–166.

14 S. Horiuchi, Y. Tokura, *Nat. Mater.* 2008, **7**, 357.

15 A. S. Tayi, A. K. Shveyd, A. C. H. Sue, J. M. Szarko, B. S. Rolczynski, D. Cao, T. J. Kennedy, A. A. Sarjeant, C. L. Stern, W. F. Paxton, W. Wu, S. K. Dey, A. C. Fahrenbach, J. R. Guest, H. Mohseni, L. X. Chen, K. L. Wang, J. F. Stoddart, S. I. Stupp, Nature 2012, **488**, 485.

16 D.-W. Fu, H.-L. Cai, Y. Liu, Q. Ye, W. Zhang, Y. Zhang, X.-Y. Chen, G. Giovannetti, M. Capone, J. Li, R.-G. Xiong, *Science* 2013, **339**, 425–428.

17 L. Wen, L. Zhou, B. Zhang, X. Meng, H. Qu, D. Li, *J. Mater. Chem.* 2012, **22**, 22603–22609.

18 X. Duan, Q. Meng, Y. Su, Y. Li, C. Duan, X. Ren, C. Lu, *Chem. Eur. J.* 2011, **17**, 9936–9943.

19 P. Jain, N. S. Dalal, B. H. Toby, H. W. Kroto, A. K. Cheetham, *J. Am. Chem. Soc.* 2008, **130**, 10450–10451.

20 G.-C. Xu, X.-M. Ma, L. Zhang, Z.-M. Wang, S. Gao, *J. Am. Chem. Soc.* 2010, **132**, 9588–9590.

21 T. Furukawa, M. Date, E. Fukada, *J. Appl. Phys.* 1980, **51**, 1135–1141.

22 W. Zhang, R.-G. Xiong, *Chem. Rev.* 2012, **112**, 1163–1195.

23 W. Zhang, H.-Y. Ye, R.-G. Xiong, *Coord. Chem. Rev.* 2009, **253**, 2980–2997.

24 S. Horiuchi, Y. Tokunaga, G. Giovannetti, S. Picozzi, H. Itoh, R. Shimano, R. Kumai, Y. Tokura, *Nature* 2010, **463**, 789.

25 X.-Y. Dong, B. Li, B.-B. Ma, S.-J. Li, M.-M. Dong, Y.-Y. Zhu, S.-Q. Zang, Y. Song, H.-W. Hou, T. C. W. Mak, *J. Am. Chem. Soc.* 2013, **135**, 10214–10217.

26 A. Yadav, P. Kulkarni, B. Praveenkumar, A. Steiner, R. Boomishankar, *Chem. Eur. J.* 2018, **24**, 14639–14643.

27 A. K. Srivastava, B. Praveenkumar, I. K. Mahawar, P. Divya, S. Shalini, R. Boomishankar, *Chem. Mater.* 2014, **26**, 3811–3817.

28 A. K. Srivastava, P. Divya, B. Praveenkumar, R. Boomishankar, *Chem. Mater.* 2015, **27**, 5222–5229.

29 A. F. Wells, *Structural Inorganic Chemistry*, Oxford University press, Oxford. **2012**.

30 H. Ma, W. Gao, J. Wang, T. Wu, G. Yuan, J. Liu, Z. Liu, *Adv. Electron. Mater.* 2016, **2**, 1600038.

31 L. Pintilie, M. Lisca, M. Alexe, *Appl. Phys. Lett.* 2005, **86**, 192902.

32 L. Filip, L. Pintilie, V. Stancu, I. Pintilie, *Thin Solid Films* 2015, **592**.

33 K. Liang, A. Buditama, D. Chien, J. Cui, P. L. Cheung, S. Goljahi, S. H. Tolbert, J. P. Chang, C. S. Lynch, *J. Appl. Phys.* 2015, **117**, 174107.

34 Q. Pan, Z.-B. Liu, H.-Y. Zhang, W.-Y. Zhang, Y.-Y. Tang, Y.-M. You, P.-F. Li, W.-Q. Liao, P.-P. Shi, R.-W. Ma, R.-Y. Wei, R.-G. Xiong, *Adv. Mater.* 2017, **29**, 1700831.

35 H. Cui, B. Zhou, L.-S. Long, Y. Okano, H. Kobayashi, H. Tanaka, *Angew. Chem. Int. Ed.* 2008, **47**, 3376–3380; *Angew. Chem.* 2008, **120**, 3424–3428.

36 M. Usman, C.-H. Lee, D.-S. Hung, S.-F. Lee, C.-C. Wang, T.-T. Luo, L. Zhao, M.-K. Wu, K.-L. Lu, *J. Mater. Chem. C* 2014, **2**, 3762–3768.

37 I. Stassen, N. Burtch, A. Talin, P. Falcaro, M. Allendorf, R. Ameloot, *Chem. Soc. Rev.* 2017, **46**, 3185–3241.

38 G. M. Sheldrick, *Acta Crystallogr. A* 2008, **64**, 112–122.